INITIAL FIBER ORIENTATION EFFECTS ON PREDICTING THERMO-MECHANICAL PROPERTIES OF LARGE VOLUME, FUSED FILAMENT COMPOSITES

Timothy Rusell, David Jack
Baylor University

Abstract

The addition of short reinforcing fibers to a 3D printing polymer feedstock can help improve the structural and thermal properties of a 3D printed part. This is important in large volume 3D printing such as the Big Area Additive Manufacturing (BAAM) done by Oak Ridge National Laboratories and Cincinnati Inc., where large scale, load bearing parts are desired that maintain dimensional tolerances under a wide range of temperatures to mitigate part warpage. In addition to the increase in stiffness, carbon fibers have a low coefficient of thermal expansion (CTE) and high stiffness, making them an excellent choice for reinforcing the polymers used in the BAAM process. In this study, the effective, longitudinal stiffness and thermal expansion properties of a short fiber composite bead, fabricated with a BAAM extruder, are investigated for their sensitivity to variations in the initial fiber alignment state upstream of the nozzle outlet. The particular composite considered in this study is a 10% by weight carbon fiber filled acrylonitrile butadiene styrene (ABS). The results of the predicted fiber orientation state within the extruded bead are presented from both the Isotropic Rotary Diffusion (IRD) model and the Reduced Strain Closure (RSC) model to investigate the sensitivity of the predicted results to the fiber interaction model. Unlike typical injection molding where a large portion of the flow occurs after the inlet gate, the orientation state in the deposited bead is unchanged shortly after the die swell and subsequent deposition. Thus, there is very little flow history where the velocity gradients are constant and the fiber orientation is allowed to achieve a steady state condition. Once the orientation is quantified, the bulk stiffness and CTE tensor properties are expressed as functions of the fiber orientation state. In this paper, a comparison is made over a range of possible initial fiber orientation states to highlight the sensitivity in predictions of the effective, longitudinal Young's modulus, E_L, and effective longitudinal CTE, α_L, for each of the two fiber interaction models. The results indicate that the RSC model is far more sensitive to the initial fiber orientation state condition than the IRD model over the entire range of parameters studied.

Introduction

Over a hundred years ago, it was known that superior structural materials could be made from combining two or more materials together such as natural fibers and a matrix material [1]. Additive Manufacturing (AM), also called 3D printing, however, is a more recent innovation that began mostly with the use of virgin polymer build material. Strictly using virgin polymer limits the capability of AM in producing structurally sound parts. However, it has developed substantially over recent years and the AM industry is starting to see that 3D printing of composite materials has the potential to produce structural parts. The impact of being able to successfully and consistently manufacture composite 3D printed parts could provide significant benefits to both the automotive and aerospace industries. Carbon fibers are a useful resource for large scale 3D printing as they have a high strength-to-weight ratio and, due to their very low CTE, they help mitigate part warpage while large temperature changes occur in the 3D printing process [2]. The effective stiffness and CTE of a 3D printed composite, however, is dependent on the internal fiber orientation state. Therefore for accurate predictions of the effective stiffness and CTE, one must first predict the fiber orientation state throughout the entire manufacturing process.

Fiber Orientation Models

Current methods of predicting the fiber orientation state within a short-fiber-polymer suspension flow are built upon Jeffery's 1923 model [3], which describes the motion of a single, rigid, massless, ellipsoidal fiber in a boundless flow domain. Jeffery's model is for a single fiber and cannot be usefully applied to concentrated fiber-matrix suspensions which involve fiber-fiber interactions. Most authors use a variation of the Fokker-Planck model to represent semi-concentrated or concentrated suspensions of interacting fibers to capture the orientation state.

The IRD Model

Folgar and Tucker investigated concentrated fiber-matrix suspensions with their Isotropic Rotary Diffusion (IRD) model [4] in which they added a fiber interaction term, C_I, to Jeffery's original model. When using an orientation tensor approach, popularized by Advani and Tucker [5], the IRD model can be represented with the following equation,

$$\frac{\mathrm{D}\mathbf{A}}{\mathrm{Dt}} = -\frac{1}{2}(\mathbf{\Omega}\cdot\mathbf{A} - \mathbf{A}\cdot\mathbf{\Omega}) + \frac{1}{2}\lambda(\mathbf{\Gamma}\cdot\mathbf{A} + \mathbf{A}\cdot\mathbf{\Gamma} - 2\mathbf{A_4}\colon\mathbf{\Gamma}) + 2C_I\dot{\gamma}(\mathbf{I} - 3\mathbf{A}) \tag{1}$$

Equation (1) describes the change in the overall orientation state of many fibers with respect to time. In this equation, $\mathbf{A}$ and $\mathbf{A_4}$ represent, respectively, the second and fourth order orientation tensors defined as

$$\mathbf{A} = \int_S \mathbf{pp}\psi(\mathbf{p},t)\mathrm{d}\mathbf{p},\ \ \mathbf{A_4} = \int_S \mathbf{pppp}\psi(\mathbf{p},t)\mathrm{d}\mathbf{p} \tag{2}$$

where $\mathbf{p}$ is a directional unit vector pointing along the length of a fiber, the integrals are taken over the unit sphere noted by S, and ψ is the fiber orientation probability density function [5]. The vorticity and rate of deformation tensors are given as $\mathbf{\Omega} = (\nabla\mathbf{v})^{\mathrm{T}} - \nabla\mathbf{v}$ and $\mathbf{\Gamma} = (\nabla\mathbf{v})^{\mathrm{T}} + \nabla\mathbf{v}$, respectively, where the velocity gradients are defined as $(\nabla\mathbf{v})_{ij} = \frac{\partial v_i}{\partial x_j}$, $\dot{\gamma} = \sqrt{\frac{1}{2}\mathbf{\Gamma}\colon\mathbf{\Gamma}}$ is the magnitude of the rate of deformation tensor, and $\mathbf{I}$ is the second order identity tensor.

The shape of the fiber is taken into account in Equation (1) through the term $\lambda = \frac{r_e^2-1}{r_e^2+1}$, where r_e is the equivalent ellipsoidal aspect ratio. Since Jeffery's model was originally made for ellipsoidal particles, an equivalent ellipsoidal aspect ratio must be used instead of the geometric aspect ratio ($a_r = length/diameter$) when modeling other axisymmetric-shaped fibers such as cylinders [6,7]. For this study, the fibers are assumed to be cylindrical and the equation for the equivalent ellipsoidal aspect ratio is given as (see e.g. [7])

$$r_e = 0.000035a_r^3 - 0.00467a_r^2 + 0.764a_r + 0.404 \tag{3}$$

where $a_r = length/diameter$ is the geometric aspect ratio.

In this paper, a single dot represents the dot product and the colon operator represents a double contraction. The fourth order orientation tensor ($\mathbf{A_4}$) in Equation (1) is usually approximated in terms of the second order orientation tensor ($\mathbf{A_4} \approx f(\mathbf{A})$) using a closure method. The research done on closure methods is extensive (see e.g. [5,8–13] for a small sampling of models available in the literature). An orthotropic closure [8] is used in this particular study. It is worth noting that although an evolution equation for ψ (which is a complete description of the orientation state) could be solved numerically, it is computationally cumbersome. Orientation tensors are compact and allow for greater computational efficiency (see e.g. [5]).

Without the $2C_I\dot{\gamma}(\mathbf{I} - 3\mathbf{A})$ term, Equation (1) reduces to the orientation tensor form of Jeffery's

equation as long as the exact closure of Montgomery-Smith et al. [12] is used for $\mathbf{A_4}$. With the appearance of the interaction term in Equation (1), the fiber orientation state is more randomized and the periodic motion predicted by Jeffery's model, termed "Jeffery orbits," is dampened such that the fiber orientation state will approach a steady state value.

The RSC Model

Based on the standard IRD model, the RSC model was developed to improve upon the transient prediction of the fiber orientation state made by the IRD. That is, the IRD model predicts that the steady fiber orientation state will be reached more quickly than experiments suggest. To address this, the RSC model slows down the rate of alignment while predicting nearly the exact same steady state solution as the IRD model in shearing flows [14]. The RSC model [14] can be expressed in orientation tensor form as

$$\frac{\mathrm{D}\mathbf{A}}{\mathrm{Dt}} = -\frac{1}{2}(\boldsymbol{\Omega}\cdot\mathbf{A}-\mathbf{A}\cdot\boldsymbol{\Omega}) + \frac{1}{2}\lambda\{\boldsymbol{\Gamma}\cdot\mathbf{A}+\mathbf{A}\cdot\boldsymbol{\Gamma}-2\boldsymbol{\Gamma}[\mathbf{A_4}+(1-\kappa)(\mathbf{L_4}-\mathbf{M_4}\colon\mathbf{A_4})]\} + 2\kappa C_I\dot{\gamma}(\mathbf{I}-3\mathbf{A}) \tag{4}$$

Equation (4) is identical to Equation (1), except that the $2\mathbf{A_4}\colon\boldsymbol{\Gamma}$ term in Equation (1) has been replaced with $2\boldsymbol{\Gamma}[\mathbf{A_4}+(1-\kappa)(\mathbf{L_4}-\mathbf{M_4}\colon\mathbf{A_4})]$ in Equation (4) and the fiber interaction term has been multiplied by κ in Equation (4). The κ parameter is between 0 and 1 and functions to slow down the rate of alignment as $\kappa \to 0^+$. One should notice that $\kappa = 1$ will make the RSC model equivalent to the IRD model. The two other new terms in Equation (4) are defined as

$$\mathbf{L_4} = \sum_{i=1}^{3}\lambda_i\boldsymbol{e}_i\boldsymbol{e}_i\boldsymbol{e}_i\boldsymbol{e}_i,\ \ \mathbf{M_4} = \sum_{i=1}^{3}\boldsymbol{e}_i\boldsymbol{e}_i\boldsymbol{e}_i\boldsymbol{e}_i \tag{5}$$

where λ_i and $\boldsymbol{e}_i$ are the ith eigenvalue and eigenvector of $\mathbf{A}$, respectively.

Predicting Thermo-Mechanical Properties

The thermo-mechanical properties, specifically the stiffness and CTE tensor properties, of a short-fiber composite are dependent on the internal fiber orientation state. Once the stiffness and CTE tensor properties are found, the effective longitudinal Young's modulus and CTE may be found.

The Stiffness Tensor

The spatially varying, homogenized, fourth order stiffness tensor can be found as a function of $\mathbf{A}$ and $\mathbf{A_4}$, according to Advani and Tucker [5], with the equation

$$\langle C_{ijkl}\rangle = B_1A_{ijkl} + B_2\big(A_{ij}I_{kl}+A_{kl}I_{ij}\big) + B_3\big(A_{ik}I_{jl}+A_{il}I_{jk}I_{jl}+A_{jl}I_{ik}I_{jl}+A_{jk}I_{il}\big) + B_4\big(I_{ij}I_{kl}\big) + B_5(I_{ik}I_{jl}+I_{il}I_{jk}) \tag{6}$$

In Equation (6), $\langle C_{ijkl}\rangle$ is the (i,j,k,l) component of the homogenized stiffness tensor, A_{ijkl} is the (i,j,k,l) component of $\mathbf{A_4}$, A_{ij} is the (i,j) component of $\mathbf{A}$, I_{ij} is the (i,j) component of the second order identity tensor, and the B_i's are

$$\begin{aligned} B_1 &= \overline{C}_{1111}+\overline{C}_{2222}-2\overline{C}_{1122}-4\overline{C}_{1212} & B_4 &= \overline{C}_{2233} \\ B_2 &= \overline{C}_{1122}-\overline{C}_{2233} & B_5 &= 0.5(\overline{C}_{2222}+\overline{C}_{2233}) \\ B_3 &= \overline{C}_{1212}+0.5(\overline{C}_{2233}-2\overline{C}_{2222}) \end{aligned} \tag{7}$$

In Equation (7), $\overline{C}_{ijkl}$ is the (i,j,k,l) component of the unidirectional composite stiffness tensor in

the reference frame oriented along the fiber direction. The underlying stiffness tensor of the unidirectional composite is found in this study according to Tandon and Weng's micromechanics model [15]. $\mathbf{A_4}$ is approximated in Equation (6) using the same closure used in Equations (1) and (4) – that of the orthotropic closure of VerWeyst [9].

The Coefficient of Thermal Expansion Tensor

The CTE tensor can be found according to [16] with the equation

$$\langle \alpha_{ij} \rangle = \langle C_{ijkl} \alpha_{ij} \rangle \langle C_{ijkl} \rangle^{-1} \tag{8}$$

where $\langle C_{ijkl} \rangle^{-1}$ is the inverse of the stiffness tensor found in Equation (6) and

$$\langle C_{ijkl} \alpha_{ij} \rangle = D_1 A_{ij} + D_2 I_{ij} \tag{9}$$

where A_{ij} and I_{ij} are defined as before and

$$\begin{aligned} D_1 &= A_1(B_1 + B_2 + 4B_3 + B_5) + A_2(B_1 + 3B_2 + 4B_3) \\ D_2 &= A_1(B_2 + B_4) + A_2(B_2 + 3B_4 + B_5) \end{aligned} \tag{10}$$

In Equation (10), the B_i values are defined as in Equation (7) and

$$\begin{aligned} A_1 &= \bar{\alpha}_{11} - \bar{\alpha}_{22} \\ A_2 &= \bar{\alpha}_{22} \end{aligned} \tag{11}$$

In Equation (11), the $\bar{\alpha}_{ij}$ values are the CTE tensor components of a unidirectional composite aligned along the x_1 axis. The CTE tensor of the unidirectional composite is found according to Schapery's method [17] as presented by Stair and Jack [18].

Computational Methodology

There are three phases to the computational methodology used in this study. The first phase includes defining the flow domain and the resulting finite element formulation in COMSOL Multiphysics (Version 5.3; COMSOL Inc., Stockholm, Sweden, 2017). The result yields the velocity profile in this flow domain. The next phase is to solve for the fiber orientation state given the velocity profile found in the first phase (thus, the fiber orientation state is decoupled from altering the flow profile). This is done in MATLAB (R2016a; MathWorks, 2016) wherein the IRD and RSC models have been programmed. After the completion of this phase, one will have found the predicted fiber orientation state in the deposited, composite, 3D printed bead. Thus, one can repeat the process with different initial orientation states to see how strongly the initial orientation state effects the final orientation state. The third and final phase of this study goes one step further and involves predicting the effective longitudinal stiffness and CTE of the printed, composite bead. This final phase allows one to quantify the discrepancy in predictions caused by varying the initial orientation state. The values used for the Young's modulus, Poisson's ratio, and CTE of the ABS matrix in this study were $2.25\ GPa$, 0.35, and $90 \times 10^{-6}\ (^oC)^{-1}$, and for the carbon fiber they were $230\ GPa$, 0.2, and $-2.6 \times 10^{-6}\ (^oC)^{-1}$. The density of the carbon fiber and ABS were taken to be $1700\ kg/m^3$ and $1040\ kg/m^3$, respectively, and the fiber weight fraction was taken to be 10%. Finally, the geometric aspect ratio used was 20 which is reasonable for short carbon fiber reinforcements [19].

Finite Element Flow Model

The flow domain defined in the finite element solver is for a 2D planar flow and the dimensions

are similar to those of a large volume, 3D printer nozzle. The flow domain includes the flow in the nozzle and the subsequent die swell and deposition onto the print bed. The model can be seen, with dimensions and boundary conditions also defined, in Figures 1(a) and (b).

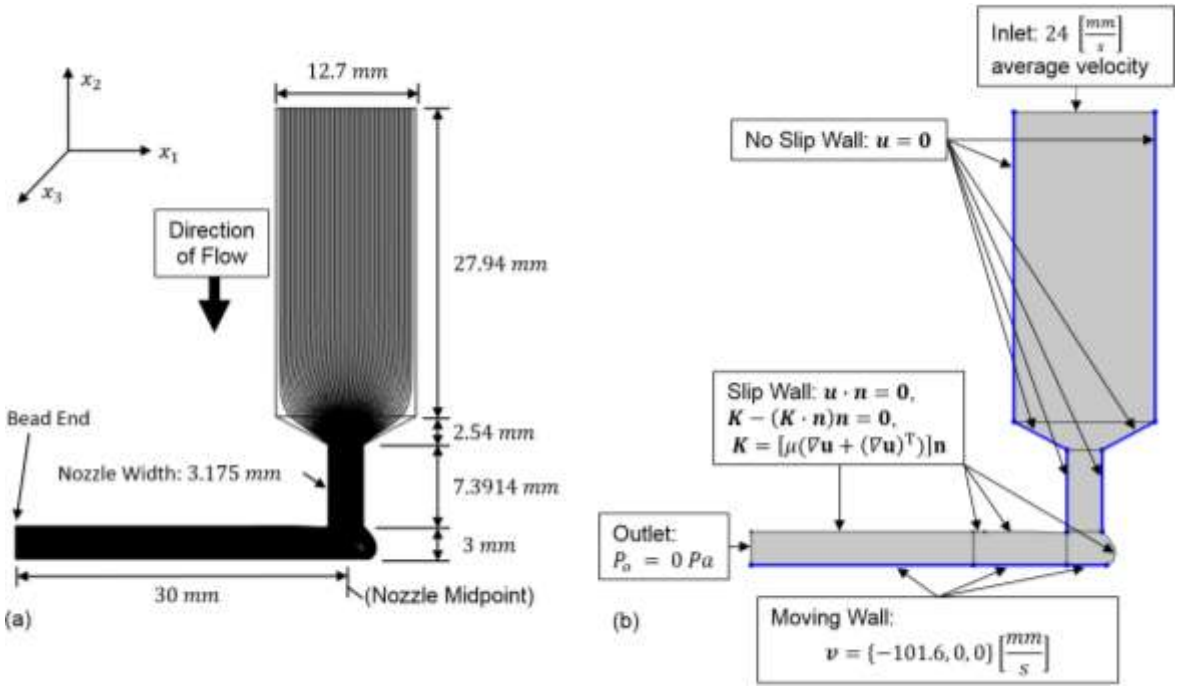

Figure 1: Finite Element Model of the Flow Domain

The flow enters the top of the domain with an average velocity of $24\ mm/s$. The walls of the nozzle have a no slip condition, meaning the displacement vector is zero ($\boldsymbol{u} = \mathbf{0}$) along the walls. After exiting the nozzle, the polymer swells. The shape of the die-swell is generated according to the method by Heller et al. [20,21]. The exposed surface of the bead after exiting the nozzle is considered to be a slip wall and the surface in contact with the print bed is considered to be a moving wall with a fixed velocity of $101.6\ mm/s$ in the $-x_1$ direction. The "outlet" of the flow domain is the end of the printed bead and is constrained to have a pressure of $0\ Pa$. The flow is considered to be a Newtonian fluid under Stokes flow with inertial effects neglected.

The finite element solver was used to solve for the velocity profile of the flow using a finite element mesh with over 1600 elements. In addition, the velocities in the x_1 and x_2 directions, v_1 and v_2, respectively, along with the velocity gradients $\frac{\partial v_1}{\partial x_1}$, $\frac{\partial v_1}{\partial x_2}$, $\frac{\partial v_2}{\partial x_1}$, and $\frac{\partial v_2}{\partial x_2}$ were found along 61 streamlines in the flow, which are shown in Figure 1(a). After solving, the velocity and velocity gradient data generated by the finite element solver was exported to `*.txt` files to be loaded and used in MATLAB for the fiber orientation analysis.

Fiber Orientation Analysis

Once the velocity and velocity gradient data are found using the finite element package, a custom MATLAB code is used to predict the fiber orientation state, designated by the second order orientation tensor $\mathbf{A}$, and the resulting stiffness and CTE tensors at each spatial location in the flow domain. Two functions were written for predicting the fiber orientation state – one for the IRD model in the form of Equation (1) and the other for the RSC model in the form of Equation (4). Results for the IRD model with $C_I = 0.01$ and an initial orientation of $\mathbf{A}_0 = 1/3 \cdot \mathbf{I}$ are shown

in Figure 2(a) for illustrative purposes. Figure 2(a) shows a few components of $\mathbf{A}$ plotted at the end of the printed bead, as functions of the bead height (x_2). Similarly, results for the RSC model for the same $\mathbf{A}_o$ and C_I are shown in Figure 2(b) for $\kappa = 1/10$. In both instances, the orientation is on average greatest in the bead direction (x_1) but due to the slowness parameter in the RSC model, the final orientation state is drastically different between the two models. One should notice for the IRD model, with no slowness parameter, there is not much variation in properties across the thickness of the bead, but the RSC model predicts that there are.

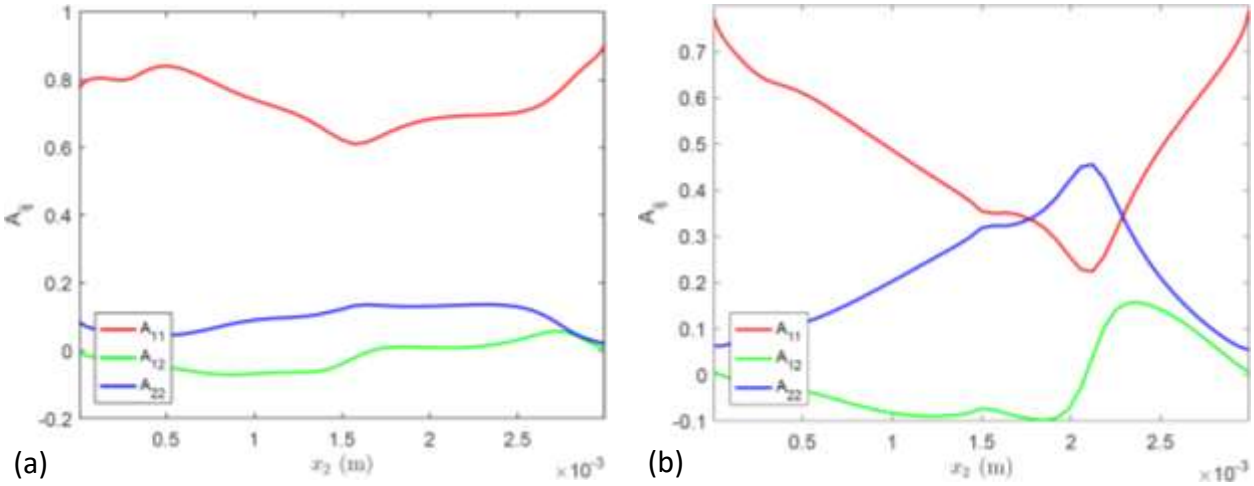

Figure 2: $\boldsymbol{A}$ in the Deposited Bead from (a) the IRD with $C_I = 0.01$, $\boldsymbol{A}_o = 1/3 \cdot \mathbf{I}$, and (b) the RSC with $C_I = 0.01$, $\kappa = 1/10$, $\boldsymbol{A}_o = 1/3 \cdot \mathbf{I}$

Once the orientation state throughout the deposited bead is known, the stiffness and CTE tensors are obtained as a function of position using a custom code that implements Equations (6) and (8). The orthotropic closure of VerWeyst was used in this study to obtain $\mathbf{A_4}$ from the orientation state for evaluating Equations (6) and (8).

Finite Element Simulations

After predicting the stiffness and CTE tensors in the bead, the finite element package is used to simulate a displacement-prescribed tensile test and a heating test for obtaining the effective longitudinal CTE using the newly found stiffness and CTE tensor properties. The samples and boundary conditions for the tensile test and the CTE test are depicted in Figures 3(a) and (b), respectively.

COMSOL is linked to MATLAB via LiveLink in this phase of the computational methodology so that it may have access to the stiffness and CTE tensors. The stiffness and CTE tensor values across the end of the printed bead (which are calculated using such $\mathbf{A}$ values as those depicted in Figure 2, for example) are used to define the respective properties across the entire x_1-dimensions of the tensile and CTE samples. For stiffness and CTE values between streamlines, we use a simple linear interpolation scheme. For the tensile simulation, a displacement of $u_1 = 0.01\ mm$ is applied in the $-x_1$ direction to the entire left side of a sample that is the same height as the deposited bead ($3\ mm$) and has an initial width of $w_o = 1.5\ mm$. The CTE sample is the exact same size as the tensile sample, has an initial temperature of $0^o C$ across its entirety, does not have any displacements or loads applied to it, and, instead, has a temperature "load" of $1^o C$ applied to its entire left side. The rest of the boundary conditions for the samples are as shown in Figure 3. A finite element mesh of 21 nodes in the x_1 direction and 61 nodes in the x_2 direction is used for both samples. After a tensile simulation was performed, the effective, longitudinal Young's modulus of the deposited, composite bead was found using the equation

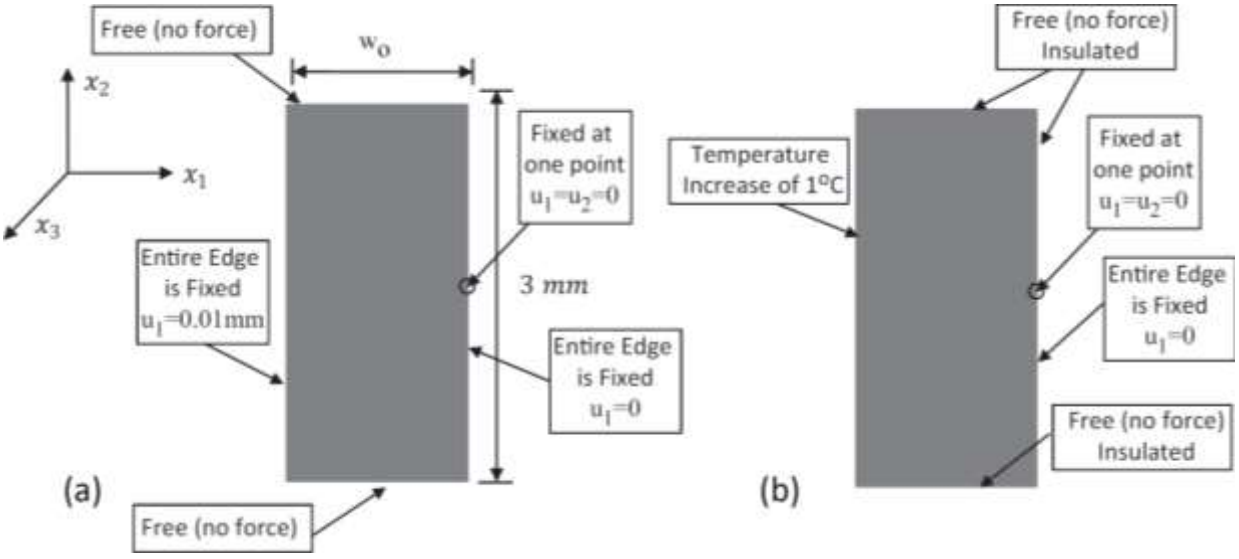

Figure 3: Finite Element Analysis Boundary Conditions: (a) Tensile Sample, and (b) CTE Sample

$$E_L = E_1 = \sigma_{11}/(u_1/w_o) \tag{12}$$

where σ_{11} is the x_1-stress on the left side of the sample, u_1 is the x_1-displacement of the left side of the sample, and w_o is the original width of the sample. The effective, longitudinal CTE was found after a CTE simulation according to the equation

$$\alpha_L = \alpha_1 = (-u_1/\Delta T)/w_o \tag{13}$$

where u_1 in this case is the resulting displacement of the x_1 face due to the increased temperature state, w_o is defined as before, the negative sign ensures α_L will be positive under expansion, and $\Delta T = 1^o C$ is the change in temperature of the sample.

Results

The computational methodology described above was followed for four different initial orientation states. The first initial condition for orientation, as is often assumed, is the random condition

$$\mathbf{A}_\mathrm{o} = 1/3 \cdot \mathbf{I} \tag{14}$$

The second initial condition studied is the "steady state" initial condition. This is found by defining a $1\ m$ long flow channel with the same width as the nozzle inlet in Figure 1. The IRD model was used to predict the orientation state at the end of the flow channel, similarly to what was done to obtain Figure 2. The long channel allowed the orientation state to become steady before reaching the end of the channel and is called the "steady state" orientation condition given as

$$\mathbf{A}_\mathrm{o} = \begin{bmatrix} 0.0771 & A_{12} & 0 \\ A_{12} & 0.7661 & 0 \\ 0 & 0 & 0.1568 \end{bmatrix} \tag{15}$$

Note, for this "steady state" initial condition, $A_{12} = -0.0788$ to the left of the center of the nozzle, 0 in the center, and 0.0788 to the right of the center. Two other initial orientation states considered include an orientation state that is highly aligned in x_2

$$\mathbf{A}_o = \begin{bmatrix} 0.0425 & 0 & 0 \\ 0 & 0.915 & 0 \\ 0 & 0 & 0.0425 \end{bmatrix} \tag{16}$$

and an orientation state that is random in the x_1-x_3 plane, given as

$$\mathbf{A}_o = \begin{bmatrix} 1/2 & 0 & 0 \\ 0 & 0 & 0 \\ 0 & 0 & 1/2 \end{bmatrix} \tag{17}$$

Figure (4) shows A_{11} and A_{22} as functions of the bead height (x_2) at the end of the printed bead for both the IRD model with $C_I = 0.01$ and the RSC model with $C_I = 0.01$ and $\kappa = 1/10$ and the initial orientation states given in Equations (14)-(17).

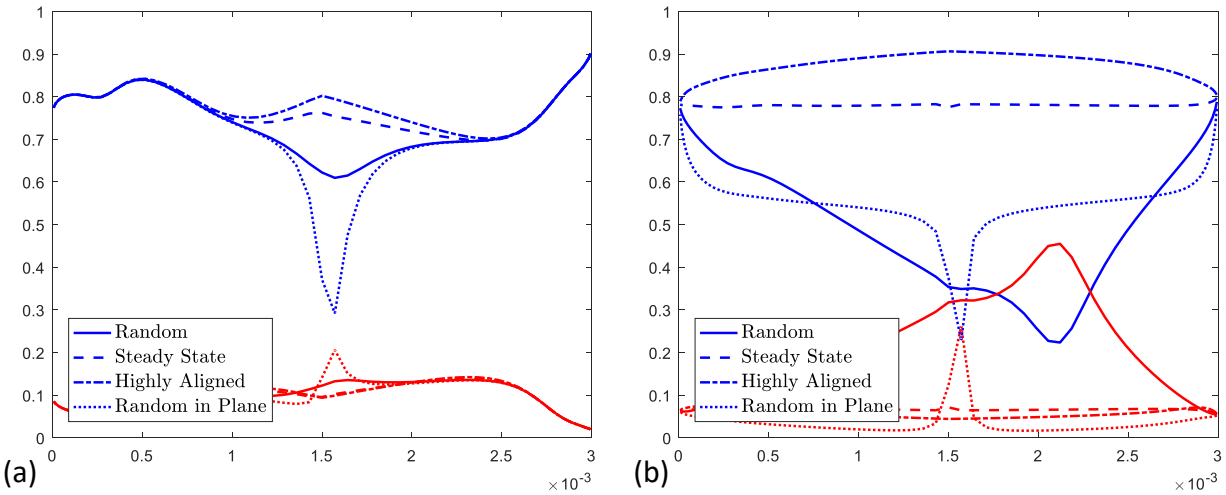

Figure 4: A_{11} (blue) and A_{22} (red) at the End of the Printed Bead (a) IRD with $C_I = 0.01$, and (b) RSC with $C_I = 0.01$ and $\kappa = 1/10$

As one can see, the changing of the initial orientation state has a much greater effect on the RSC results than the IRD results. One can also see this when the effective longitudinal stiffness (E_L) and CTE (α_L) are calculated. The impact is shown in Table 1 where E_L and α_L are compared between the differing fiber interaction models and the different initial conditions.

Table I: Predicted Effective Longitudinal Modulus and CTE of the Composite, Printed Bead

	C_I	κ	$\mathbf{A}_o$	$E_L\ (GPa)$	$\alpha_L\ (\times 10^{-6}/^oC)$
IRD	0.01	1	Random	5.73	39.0
	0.01	1	Steady state	5.94	38.1
	0.01	1	Highly aligned	6.03	37.8
	0.01	1	Random in-plane	5.59	40.0
RSC	0.01	1/10	Random	4.19	51.5
	0.01	1/10	Steady state	6.09	37.7
	0.01	1/10	Highly aligned	6.92	35.9
	0.01	1/10	Random in-plane	4.54	47.1

Table 1 shows that there is a bigger discrepancy in the predictions made using the RSC model than there is when using the IRD model. For example, the largest and smallest E_L values obtained with the IRD are $6.03\,GPa$ and $5.59\,GPa$ ($difference = 0.44\,GPa$), whereas the largest and

smallest E_L values obtained with the RSC model are $6.92\,GPa$ and $4.19\,GPa$ ($difference = 2.73\,GPa$). Likewise, the largest and smallest IRD results for α_L are $40.0 \times 10^{-6}/^oC$ and $37.8 \times 10^{-6}/^oC$ ($difference = 2.2 \times 10^{-6}/^oC$), whereas the largest and smallest α_L for the RSC are $51.5 \times 10^{-6}/^oC$ and $35.9 \times 10^{-6}/^oC$ ($difference = 15.6 \times 10^{-6}/^oC$).

One may notice that the initial orientation state that was random in the x_1-x_3 plane led to the lowest E_L, whereas the initial orientation state that was highly aligned in the x_2 direction led to the highest E_L. This is because in the initially highly aligned case the fibers are already oriented in the flow direction, whereas for the initially random in-plane case none of the fibers are aligned in the flow direction initially. Although the fibers will tend to align towards the flow direction (see e.g. [22]), the initially random in-plane case for the RSC model simply does not allow the fibers sufficient time to align in the flow direction to the degree that they do in the highly x_2-aligned case.

One may also notice that the largest E_L values pair with the smallest α_L values. This is due to the extremely low CTE value of the carbon fibers and their high stiffness – the direction of their highest alignment will be the direction of greatest stiffness but lowest CTE. The opposite is also true – the smallest E_L values tend to pair with the largest α_L values.

Summary

This study has demonstrated that the RSC model is much more sensitive than the IRD model to the initial orientation state used. Thus, although the RSC model was invented as an upgrade of the IRD model, one should be aware of this fact when choosing a fiber orientation model for industrial use. As the RSC model is considered by many authors as an improvement upon the IRD model, this flow scenario demonstrates the need to better understand the appropriate flow model.

Acknowledgements

The authors would like to thank Baylor University for funding this project. Thanks also goes to Dr. Douglas Smith and Blake Heller for the use of their die-swell model domain of the large volume, 3D printer nozzle.

Bibliography

[1] Lau, K., Hung, P., Zhu, M.-H., and Hui, D., 2018, “Properties of Natural Fibre Composites for Structural Engineering Applications,” Compos. Part B Eng., **136**, pp. 222–233.

[2] Love, L. J., Kunc, V., Rios, O., Duty, C. E., Elliott, A. M., Post, B. K., Smith, R. J., and Blue, C. A., 2014, “The Importance of Carbon Fiber to Polymer Additive Manufacturing,” J. Mater. Res. Warrendale, **29**(17), pp. 1893–1898.

[3] Jeffery, G. B., 1922, “The Motion of Ellipsoidal Particles Immersed in a Viscous Fluid,” Proc. R. Soc. Lond. Ser. Contain. Pap. Math. Phys. Character, **102**(715), pp. 161–179.

[4] Folgar, F., and Tucker, C. L., 1984, “Orientation Behavior of Fibers in Concentrated Suspensions,” J. Reinf. Plast. Compos., **3**(2), pp. 98–119.

[5] Advani, S. G., and Tucker, C. L., 1987, “The Use of Tensors to Describe and Predict Fiber Orientation in Short Fiber Composites,” J. Rheol., **31**(8), pp. 751–784.

[6] Trevelyan, B. J., and Mason, S. G., 1951, “Particle Motions in Sheared Suspensions. I. Rotations,” J. Colloid Sci., **6**(4), pp. 354–367.

[7] Zhang, D., E. Smith, D., A. Jack, D., and Montgomery-Smith, S., 2011, “Numerical Evaluation of Single Fiber Motion for Short-Fiber-Reinforced Composite Materials Processing,” J. Manuf. Sci. Eng., **133**(5), pp. 051002-051002–9.

[8] Cintra, J. S., and Tucker, C. L., 1995, “Orthotropic Closure Approximations for Flow-induced Fiber Orientation,” J. Rheol., **39**(6), pp. 1095–1122.

[9] Verweyst, B. E., and Tucker, C. L., “Fiber Suspensions in Complex Geometries: Flow/Orientation Coupling,” Can. J. Chem. Eng., **80**(6), pp. 1093–1106.
[10] Chung, D. H., and Kwon, T. H., 2001, “Improved Model of Orthotropic Closure Approximation for Flow Induced Fiber Orientation,” Polym. Compos., **\bf 22**(5), pp. 636–649.
[11] Montgomery-Smith, S., Jack, D., and Smith, D. E., 2011, “The Fast Exact Closure for Jeffery’s Equation with Diffusion,” J. Non-Newton. Fluid Mech., **166**(7), pp. 343–353.
[12] Montgomery-Smith, S., He, W., Jack, D. A., and Smith, D. E., 2011, “Exact Tensor Closures for the Three-Dimensional Jeffery’s Equation,” J. Fluid Mech., **680**, pp. 321–335.
[13] Doi, M., and Ohta, T., 1991, “Dynamics and Rheology of Complex Interfaces. I,” J. Chem. Phys., **95**(2), pp. 1242–1248.
[14] Wang, J., O’Gara, J. F., and Tucker, C. L., 2008, “An Objective Model for Slow Orientation Kinetics in Concentrated Fiber Suspensions: Theory and Rheological Evidence,” J. Rheol., **52**(5), pp. 1179–1200.
[15] Tandon, G. P., and Weng, G. J., 1984, “The Effect of Aspect Ratio of Inclusions on the Elastic Properties of Unidirectionally Aligned Composites,” Polym. Compos., **5**(4), pp. 327–333.
[16] Camacho, C. W., Tucker, C. L., Yalvaç, S., and McGee, R. L., 1990, “Stiffness and Thermal Expansion Predictions for Hybrid Short Fiber Composites,” Polym. Compos., **11**(4), pp. 229–239.
[17] Schapery, R. A., 1968, “Thermal Expansion Coefficients of Composite Materials Based on Energy Principles,” J. Compos. Mater., **2**(3), pp. 380–404.
[18] Stair, S., and Jack, D. A., 2015, “Comparison of Experimental and Modeling Results for Cure Induced Curvature of a Carbon Fiber Laminate,” Polym. Compos., p. n/a-n/a.
[19] Duty, C. E., Kunc, V., Compton, B., Post, B., Erdman, D., Smith, R., Lind, R., Lloyd, P., and Love, L., 2017, “Structure and Mechanical Behavior of Big Area Additive Manufacturing (BAAM) Materials,” Rapid Prototyp. J., **23**(1), pp. 181–189.
[20] Heller, B. P., Smith, D. E., and Jack, D. A., 2016, “Effects of Extrudate Swell and Nozzle Geometry on Fiber Orientation in Fused Filament Fabrication Nozzle Flow,” Addit. Manuf., **12**, pp. 252–264.
[21] Heller, B., Smith, D. E., and Jack, D. A., 2017, “Simulation of Planar Deposition Polymer Melt Flow and Fiber Orientation in Fused Filament Fabrication,” *Proceedings of the Solid Freeform Fabrication Symposium*, Austin, Texas, pp. 1096–1111.
[22] Tekinalp, H. L., Kunc, V., Velez-Garcia, G. M., Duty, C. E., Love, L. J., Naskar, A. K., Blue, C. A., and Ozcan, S., 2014, “Highly Oriented Carbon Fiber–Polymer Composites via Additive Manufacturing,” Compos. Sci. Technol., **105**, pp. 144–150.